Analytical covariance between the voxel intensity distribution and the power spectrum of line-intensity maps

Gabriela Sato-Polito[*] and José Luis Bernal[†]

William H. Miller III Department of Physics and Astronomy, Johns Hopkins University,
3400 North Charles Street, Baltimore, Maryland 21218, United States

The power spectrum and the voxel intensity distribution (VID) are two of the main proposed summary statistics to study line-intensity maps. We reformulate the derivation of the VID in terms of the local overdensities and derive for the first time an analytic covariance between the VID and the line-intensity mapping power spectrum. We study the features of this covariance for different experimental setups and show that we can recover similar results to simulation-based covariances. With this formalism, we also compute the cosmic variance contribution to the VID uncertainty, which we find to be subdominant with respect to the standard variance from Poisson sampling. Our results allow for general joint analyses of the VID and the line-intensity mapping power spectrum.

I. INTRODUCTION

Line-intensity mapping (LIM) has recently emerged as a promising technique to survey large cosmological volumes that has the potential to recover precise redshift information by targeting a variety of bright spectral lines [1]. Since the resulting maps capture the integrated specific intensity, these measurements are sensitive to both cosmology and astrophysics. The former is encoded in the clustering of galaxies and gas in the intergalactic medium that emit the desired signal, and the latter, in the luminosity produced by each emitter.

The most well-studied line is the 21-cm spin-flip transition in neutral hydrogen (see, e.g., Ref. [2]) and there are a variety of ongoing or planned experiments that target cosmic dawn and the epoch of reionization [3–8] and the late Universe [9–11]. In addition, several other line transitions at higher frequencies have garnered attention as probes of the different phases of the interstellar medium, such as the rotational lines of carbon monoxide (CO) [12–16], the fine-structure line of ionized carbon [17,18], Hα and Hβ [19,20], Lyman-α [21,22], and oxygen lines [19]. A vast number of experiments that target these spectral lines are already observing or currently under development (see e.g., Refs. [23–28]), with some initial constraints and tentative power spectrum detections [18,29–34].

Different methods have been proposed to extract information from line-intensity maps. While the LIM power spectrum is the most prominent statistic, the cosmological information it contains is inherently limited and degenerate with astrophysical uncertainties [35,36]. Complementary probes have been proposed to access non-Gaussian information and break degeneracies with astrophysical parameters. Among them, the voxel intensity distribution (VID), which is an estimator of the one-point probability distribution function of the temperature measured in a voxel, has been shown to be very promising [37,38]. The VID depends directly on the line-luminosity function and is more sensitive to the high-luminosity end that peaks above the instrumental noise, whereas the power spectrum is more sensitive to cosmological parameters and depends on a weighted average of luminosities that favors comparatively fainter objects.

While both the power spectrum and the VID have individually been shown to offer promising constraints on astrophysical and cosmological parameters, as well as extensions to ΛCDM (see e.g., Refs. [39–45]), the more substantial gain lies in their combination. The information contained in the LIM power spectrum and the VID are highly complimentary, and a joint analysis has been shown to significantly increase the precision of the inference of the line-luminosity function [46]. A joint analysis requires a covariance matrix to properly account for the shared information content of the observables. While Ref. [46] relied on simulations to estimate their covariance empirically, a theoretical understanding of the expected covariance between these observables is still lacking.

We derive, for the first time, an analytic covariance between the VID and the LIM power spectrum for spectral lines emitted within halos. We first reformulate the standard derivation of the VID signal by an equivalent expression that explicitly accounts for the local perturbations of the

[*]gsatopo1@jhu.edu
[†]jbernal2@jhu.edu

number of emitters—a biased tracer of the local matter overdensities. This enables us to include the effect of cosmic variance—the variance of the brightness temperature field on the scales of the size of the survey—as a contribution to the predicted statistical error of the VID, though we argue that it is generally a negligible contribution. Using the same reformulation of the VID, we compute its covariance with the LIM power spectrum. We focus on the Legendre monopole of the LIM power spectrum and in observations performed using only the autocorrelation between antennas, but this work can be straightforwardly extended for higher-order multipoles of the power spectrum or interferometers.

The derivation presented in this work shows that we can interpret the covariance between the VID and the power spectrum as the response of the power spectrum to the mean density perturbation. Since the VID depends (among other things) on the perturbation in the number density of emitters δ_h and the power spectrum depends on two powers of the temperature fluctuation δT, the resulting covariance is proportional to the bispectrum $\langle \delta_h \delta T \delta T \rangle$ integrated over two of the wave numbers. We note that the type of integrated bispectrum we derive here has been previously studied in the context of position-dependent power spectra and the matter density probability distribution function (PDF) [47,48], derived using the separate universe approach.

This paper is structured as follows. First, we introduce the theoretical modeling of the VID, the power spectrum and all the required quantities to compute their covariance in Sec. II. We discuss the reformulation of the probability distribution function of the temperature measured in a voxel as a function of the local density of emitters in Sec. III and use it to derive the cosmic variance contribution to the VID variance and the covariance between the VID and the power spectrum in Sec. IV. Finally, we conclude in Sec. V. We include a derivation of the shot noise bispectrum in Appendix A, details on the quantities required to compute the power spectrum and bispectrum in Appendix B and compare the analytic covariance derived in this work with the numerical results of Ref. [46] in Appendix C.

Throughout this work we consider the best-fit cosmological parameters from the full data set of *Planck* assuming ΛCDM [49] and adopt the following Fourier transform convention:

$$f(\boldsymbol{k}) = \int d^3\boldsymbol{x} f(\boldsymbol{x}) e^{-i\boldsymbol{k}\boldsymbol{x}}, \qquad f(\boldsymbol{x}) = \int \frac{d^3\boldsymbol{k}}{(2\pi)^3} f(\boldsymbol{k}) e^{i\boldsymbol{k}\boldsymbol{x}}. \tag{1.1}$$

II. THEORETICAL MODELING

In this section we briefly review the modeling of the VID and the power spectrum, as well as the quantities that will be necessary for the calculation of the variance of the VID and the covariance between the VID and the power spectrum. We begin by assuming that the measured line emission is sourced within dark matter halos, which trace the underlying matter distribution, and relate the line luminosity to halo mass.

The brightness temperature T at a position $\boldsymbol{x}$ of a given emission line with rest-frame frequency ν is related to its local luminosity density ρ_L as

$$T(\boldsymbol{x}) = \frac{c^3(1+z)^2}{8\pi k_B \nu^3 H(z)} \rho_L(\boldsymbol{x}) \equiv X_{\mathrm{LT}}\rho_L(\boldsymbol{x}), \tag{2.1}$$

where c is the speed of light, z is the redshift of the emission, k_B is the Boltzmann constant, H is the Hubble parameter and we have defined X_{LT} in the second equality to compress our expressions. The luminosity density can be computed assuming a relation between the specific luminosity L and the halo mass M. Thus, we can write the mean of the temperature distribution as

$$\langle T \rangle = X_{\mathrm{LT}} \int dM L(M) \frac{dn}{dM}, \tag{2.2}$$

where dn/dM is the halo mass function.

A. VID

The VID is the histogram of temperatures measured within the observed voxels; we follow Ref. [38] to compute it. A voxel of volume V_{vox} that contains N emitters will, in the absence of noise, have a brightness temperature of

$$T = \frac{X_{\mathrm{LT}}}{V_{\mathrm{vox}}} \sum_{i=1}^{N} L_i, \tag{2.3}$$

where L_i is the luminosity of the ith emitter. Hence, the probability of observing a temperature T for a voxel that contains only a single emitter is given by

$$\mathcal{P}_1(T) = \frac{V_{\mathrm{vox}}}{\bar{n} X_{\mathrm{LT}}} \frac{dn}{dL}\bigg|_{L=TV_{\mathrm{vox}}/X_{\mathrm{LT}}}, \tag{2.4}$$

where $\bar{n}$ is the mean comoving number density of emitters and dn/dL is the luminosity function of the targeted line, which we compute from the halo mass function and the $L(M)$ relation. We assume a mean-preserving logarithmic scatter with standard variable σ_L in the $L(M)$ relation. Then, we can obtain the luminosity function by integrating over mass:

$$\frac{dn}{dL} = \int dM \frac{dn}{dM} \frac{1}{\sqrt{2\pi}L\tilde{\sigma}_L}$$
$$\times \exp\left\{-\frac{(\log(L) - \log(L(M)) + \tilde{\sigma}_L^2/2)^2}{2\tilde{\sigma}_L^2}\right\}, \tag{2.5}$$

where we have defined $\tilde{\sigma}_L \equiv \log(10)\sigma_L$.[1] Since the contribution of each emitter to the observed temperature is additive, the probability of observing a given temperature in a voxel with N emitters is $\mathcal{P}_1$ convolved N times with itself. Similarly, in voxels where there are no emitters we have $\mathcal{P}_0(T) = \delta_D(T)$, where δ_D is the Dirac delta.

The total PDF $\mathcal{P}(T)$ of observing a voxel with temperature T is therefore given by the probability $\mathcal{P}(N)$ that a voxel contains N sources and that these N sources produce an aggregate temperature T, summed over all possible values of N. That is,

$$\mathcal{P}(T) = \sum_{N=0}^{\infty} \mathcal{P}_N(T)\mathcal{P}(N). \tag{2.6}$$

If the sources are unclustered, $\mathcal{P}(N)$ is a Poisson distribution $\mathcal{P}_{\mathrm{Poiss}}(N, \bar{N}_h)$, where the mean number $\bar{N}_h$ of emitters in a voxel is determined by the mean number density of dark matter halos in the Universe, $\bar{N}_h = \bar{n}_h V_{\mathrm{vox}}$. To include the effect of clustering in the calculation of $\mathcal{P}(N)$, Ref. [38] used the fact that the halo number count follows the matter distribution, which can be approximated by a log-normal distribution [50]. The number of emitters is then a Poisson draw where the mean is now determined by the expected number of (log-normally distributed) emitters in a given voxel. Under these assumptions, we have

$$\mathcal{P}(N) = \int d\eta \mathcal{P}_{\mathrm{LN}}(\eta)\mathcal{P}_{\mathrm{Poiss}}(N, \eta), \tag{2.7}$$

where η refers to the expected number of emitters and $\mathcal{P}_{\mathrm{LN}}$ denotes a log-normal distribution for η, assuming that the halo number count fluctuations can be expressed in terms of a Gaussian random variable and its variance [51].

Finally, the total observed temperature also includes the thermal noise (in addition to the contribution of continuum foregrounds and line interlopers, which we neglect in this work). Therefore, the total probability distribution function is

$$\mathcal{P}_{\mathrm{tot}}(T) = (\mathcal{P}_{\mathrm{noise}} * \mathcal{P})(T), \tag{2.8}$$

where usually $\mathcal{P}_{\mathrm{noise}}$ is a Gaussian distribution with standard deviation given by the effective instrumental noise per voxel and $*$ denotes the convolution operator.

The probability of observing a voxel temperature within a given range $\Delta T_i \equiv (T_i^{\mathrm{min}}, T_i^{\mathrm{max}}]$ can be estimated with the VID $\mathcal{B}_i$, which is the total number of voxels with an observed temperature within ΔT_i. The relation between $\mathcal{B}_i$, which is the actual observable, and $\mathcal{P}(T)$ is

---

[1]Note that if there is any further dispersion in any of the steps taken to obtain $L(M)$, it must be added accordingly to σ_L.

$$\mathcal{B}_i = N_{\mathrm{vox}} \int_{\Delta T_i} dT \mathcal{P}_{\mathrm{tot}}(T), \tag{2.9}$$

where $N_{\mathrm{vox}} = V_{\mathrm{field}}/V_{\mathrm{vox}}$ is the total number of voxels in an observed volume V_{field}.

B. Correlations

The total observed LIM power spectrum consists of three components—clustering, shot noise, and instrument noise—which we can write as

$$\tilde{P}_{TT}^{\mathrm{tot}}(k, \mu, z) = \tilde{P}_{TT}^{\mathrm{clust}}(k, \mu, z) + \tilde{P}_{TT}^{\mathrm{shot}}(k, \mu, z) + P^{\mathrm{N}}(z), \tag{2.10}$$

where the tilde denotes an observed quantity and μ is the cosine of the angle between the wave number vector $\boldsymbol{k}$ and the line of sight. The observed power spectrum differs from the predicted one due to the limited experimental resolution and the volume probed; this is why the observed contribution from shot noise also depends on k and μ. Hence, we include the window functions that model these limitations in the observed power spectrum, such that, for any power spectrum,

$$\tilde{P}(k, \mu) = \int \frac{\boldsymbol{q}}{(2\pi)^3} W_{\mathrm{vol}}^2(\boldsymbol{k}) W_{\mathrm{vox}}^2(\boldsymbol{q} - \boldsymbol{k}) P(\boldsymbol{q} - \boldsymbol{k}), \tag{2.11}$$

where W_{vol} models the limited survey volume and W_{vox} models the voxel resolution. We will discuss the particular forms chosen for these functions in more detail in Sec. II C. However, we note that, since the volume window simply includes or excludes certain spatial positions, it corresponds to a product with the density field in configuration space and therefore a convolution in Fourier space. Conversely, the voxel window captures the loss of information on scales smaller than the voxel size and therefore this smoothing is added as a convolution in configuration space and as a product in Fourier space.

Since the line emission is sourced within dark matter halos, the temperature fluctuations are a biased tracer of the matter distribution. We consider a simple linear bias model to describe the relation between temperature and matter perturbations and assume Poisson shot noise. We therefore model the LIM power spectrum as

$$\begin{aligned} P_{TT}(k, \mu, z) &\equiv P_{TT}^{\mathrm{clust}}(k, \mu, z) + P_{TT}^{\mathrm{shot}}(z) \\ &= \langle T \rangle^2 (b_1^T + f\mu)^2 P_l + \langle T^2 \rangle \end{aligned} \tag{2.12}$$

where P_l is the linear power spectrum of cold dark matter and baryons, b_1^T is the linear bias parameter of the temperature field, and f is the linear scale-independent growth rate. We discuss the noise power spectrum P_N in Sec. II C. Note that the average in temperature is taken over the mass distribution of halos, as in Eq. (2.2). Therefore, the second

term in Eq. (2.12) is the second moment of the temperature over the mass distribution, which corresponds to $\langle T^2 \rangle \equiv X_{LT}^2 \int dM L^2(M) dn/dM$.

The key ingredient for the calculation of the covariance between the VID and the power spectrum is a bispectrum of the form $\langle \delta_h \delta T \delta T \rangle$. This bispectrum includes contributions from clustering and shot noise, but does not have any contribution from instrumental noise since the temperature fluctuations due to thermal noise are uncorrelated with the halo density. The total bispectrum is given by

$$B_{hTT}(\boldsymbol{k}_1, \boldsymbol{k}_2, \boldsymbol{k}_3) = B_{hTT}^{clust}(\boldsymbol{k}_1, \boldsymbol{k}_2, \boldsymbol{k}_3) + \frac{P_{TT}^{clust}(\boldsymbol{k}_2) + P_{TT}^{clust}(\boldsymbol{k}_3)}{\bar{n}}$$
$$+ \langle T^2 \rangle \left(\frac{P_{hT}^{clust}(\boldsymbol{k}_1)}{\langle T \rangle} + \frac{1}{\bar{n}} \right). \quad (2.13)$$

The last two terms of the bispectrum correspond to shot noise contributions, which we assume to be Poissonian; we include their derivation in Appendix A. Using standard perturbation theory (see, e.g., Ref. [52]), we compute the power spectra and bispectrum due to clustering at tree level. We show in Appendix B the perturbation theory kernels including the effect of redshift-space distortions and the bias model assumed here.

C. Noise and survey specifications

LIM experiments measure a limited volume of the Universe and can resolve temperature fluctuations up to a limited resolution. We assume the size of the voxel to be determined by the spectral and angular resolutions, with corresponding spatial dimensions along and across the line of sight

$$\sigma_{\parallel} = \frac{c\delta\nu(1+z)}{H(z)\nu_{obs}}, \quad \sigma_{\perp} = D_M(z)\theta_{FWHM}/\sqrt{8\log 2}, \quad (2.14)$$

where $\delta\nu$ is the spectral resolution, ν_{obs} is the observed frequency, D_M is the comoving angular diameter distance, and θ_{FWHM} is the full-width at half maximum of the telescope beam. We model the effect of the angular and spectral resolutions through the window W_{vox} introduced in Eq. (2.11) and, as in Ref. [53], assume a Gaussian function in Fourier space.

We consider a cylindrical survey volume aligned with the line of sight, with side $L_{\parallel} = c\Delta\nu(1+z) \times (H\nu_{obs})$ and base with radius $R_{\perp} = D_M \sqrt{\Omega_{field}/\pi}$ (where $\Delta\nu$ and Ω_{field} are the experimental frequency bandwidth and observed solid angle, respectively). We assume that all spatial positions within the survey are observed with the same efficiency, and hence we consider the survey mask or volume window function W_{vol} to be a top hat in configuration space with values 1 and 0 for points within and outside this volume, respectively.

Finally, we assume Gaussian instrumental noise, such that the noise power spectrum P_N is given by

$$P_N = V_{vox} \sigma_N^2, \quad \text{and} \quad \sigma_N = \frac{T_{sys}}{\sqrt{N_{feeds} \delta\nu t_{pix}}}, \quad (2.15)$$

where σ_N is the standard deviation of the instrumental noise per voxel, T_{sys} is the system temperature of the telescope (though it can effectively include other limitations and contaminants such as continuum foregrounds [54]), N_{feeds} is the total effective number of detectors used, and t_{pix} is the observing time per pixel.

We choose to center our analysis on the COMAP [23] instrument and consider the CO(1-0) emission line observed at 29.6 GHz for a finished first phase of the experiment. Our fiducial experimental setup follows the expected sensitivities after 5 years of observations, which can be estimated from the early science sensitivities of COMAP [54]. We consider a single 4 deg^2 survey area with a bandwidth of 7.7 GHz (which corresponds to the redshift range $z \in 2.4$–3.4) observed during a total time of 1000 hours (effectively accounting for ~300 hours of observation in three different fields for the real experiment) with 38 effective detectors (19 feeds with double polarization), with an effective system temperature of 45 K and spectral and angular resolutions of $\delta\nu = 31.25$ MHz and $\theta_{FWHM} = 4.5$ arcmin. Finally, in order to account for the upgrade in sensitivity between the recent early science sensitivities of COMAP and the finished COMAP Y5, we use the factor $\sigma_N^{(Y5)} = \sigma_N^{(Y1)}/\sqrt{69.4}$ [54].

For the mean relation between luminosity and halo mass, we assume the fiducial COMAP model [55]:

$$\frac{L_{CO}}{L_\odot}(M) = 4.9 \times 10^{-5} \frac{C}{(M/M_\star)^A + (M/M_\star)^B}, \quad (2.16)$$

and include a mean-preserving logarithmic scatter σ_L. The fiducial values adopted by COMAP for these parameters, grounded in results from Universe Machine [56], COLDz [57] and COPSS [58], are $A = -2.85$, $B = -0.42$, $C = 10^{10.63}$, $M_\star = 10^{12.3} M_\odot$ and $\sigma_L = 0.42$. This scatter results in the luminosity function extending towards very low luminosities. We neglect the contribution from line broadening due to peculiar velocities [59] and, in order to ease the computations of $\mathcal{P}_1$ and other quantities depending on it, we impose an exponential cutoff in the luminosity function at $20 L_\odot$ which does not affect the mean luminosity; we compute $\bar{n}$ including this cutoff.

III. POSITION-DEPENDENT PDF

The temperature PDF shown in Eq. (2.6) accounts for the global matter distribution [as given in Eq. (2.7)]; however, in a finite volume of the Universe, one can expect this PDF to vary. To account for this position dependence, we

begin by rewriting Eq. (2.6) as a probability conditioned by the halo density perturbation field δ_h^{v} smoothed over a voxel:

$$P(T|\delta_h^{\text{v}}(\boldsymbol{x})) = \sum_{N=0}^{\infty} P_N(T) P(N|\delta_h^{\text{v}}(\boldsymbol{x})), \qquad (3.1)$$

where the probability $P(N|\delta_h^{\text{v}}(\boldsymbol{x}))$ is a Poisson sampling with the mean determined by the density field at a given position through $N(\boldsymbol{x}) = \bar{N}_h[1 + \delta_h^{\text{v}}(\boldsymbol{x})]$ and the smoothed halo density perturbations are

$$\delta_h^{\text{v}}(\boldsymbol{x}) = \int \mathrm{d}^3 x' W_{\text{vox}}(\boldsymbol{x} - \boldsymbol{x}') \delta_h(\boldsymbol{x}'), \qquad (3.2)$$

where δ_h is the unsmoothed field.

In principle, the probability $P(T)$ of measuring a temperature T is given by the average of $P(T|\delta_h^{\text{v}}(\boldsymbol{x}))$ over realizations of the density field. However, we can write this as a spatial average by invoking the ergodic hypothesis:

$$P(T) = \int \mathrm{d}\delta_h^{\text{v}} P(\delta_h^{\text{v}}) P(T|\delta_h^{\text{v}}) = \frac{1}{V_{\text{field}}} \int_{V_{\text{field}}} \mathrm{d}^3 x P(T|\delta_h^{\text{v}}(\boldsymbol{x})).$$

$$(3.3)$$

Equation (3.3) allows us to express $P(T)$ with an explicit dependence on the local overdensities, as will be required later in order to relate it with the power spectrum. However, this alternative derivation of $P(T)$ is completely equivalent to the standard one discussed in the previous section, under the same set of assumptions. Let us rewrite Eq. (3.3) expanding all the terms:

$$P(T) = \sum_{N=0}^{\infty} P_N(T) \int \mathrm{d}\delta_h^{\text{v}} P(\delta_h^{\text{v}}) P(N|\delta_h^{\text{v}})$$

$$= \sum_{N=0}^{\infty} P_N(T) \int \mathrm{d}\eta P(\eta) P(N|(\eta - \bar{N})/\bar{N}), \quad (3.4)$$

where the last equality just involves the change in variable from δ_h^{v} to η. Then, identifying $P(N|(\eta - \bar{N}_h)/\bar{N}_h)$ as $P_{\text{Poiss}}(N, \eta)$, we recover Eq. (2.7) if we assume a log-normal distribution for η. Although we will use Eq. (2.7) to compute the expected $P(T)$ we will stick to the expression in Eq. (3.3) to derive the covariances.

We can expand $P(N|\delta_h^{\text{v}}(\boldsymbol{x}))$ for small δ_h^{v} as

$$P(N|\delta_h^{\text{v}}(\boldsymbol{x})) = \frac{(\bar{N}_h[1 + \delta_h^{\text{v}}(\boldsymbol{x})])^N e^{-\bar{N}_h[1 + \delta_h^{\text{v}}(\boldsymbol{x})]}}{N!}$$

$$\approx \frac{\bar{N}_h^N e^{-\bar{N}_h}}{N!} \left[1 + \delta_h^{\text{v}}(\boldsymbol{x})(N - \bar{N}_h) + \frac{(\delta_h^{\text{v}})^2(\boldsymbol{x})}{2} (\bar{N}_h^2 - 2\bar{N}_h N + (N-1)N) \right]. \qquad (3.5)$$

Notice that in the last equality the term that factors out is the Poisson distribution $P_{\text{Poiss}}(N, \bar{N}_h)$. As noted in Eq. (2.8), the instrumental noise is added to the VID prediction as a convolution between the astrophysical signal and the noise PDF. This only applies to $P_N(T)$, since it is the only temperature-dependent term. Therefore, the total VID to linear order in δ_h^{v} is

$$\mathcal{B}_i = \frac{N_{\text{vox}}}{V_{\text{field}}} \int_{\Delta T_i} \mathrm{d}T \int_{V_{\text{field}}} \mathrm{d}^3 x \sum_{N=0}^{\infty} (P_{\text{noise}} * P_N)(T) P_{\text{Poiss}}(N, \bar{N}_h)[1 + \delta_h^{\text{v}}(\boldsymbol{x})(N - \bar{N}_h)]. \qquad (3.6)$$

We can write the spatial integral over the survey volume in the equation above as an integral over all space multiplied by the survey mask function $W_{\text{vol}}(\boldsymbol{x})$. Transforming to Fourier space, we have

$$\int_{V_{\text{field}}} \mathrm{d}^3 x \delta_h^{\text{v}}(\boldsymbol{x}) = \int \mathrm{d}^3 x W_{\text{vol}}(\boldsymbol{x}) \delta_h^{\text{v}}(\boldsymbol{x}) = \int \frac{\mathrm{d}^3 k}{(2\pi)^3} W_{\text{vol}}(\boldsymbol{k}) W_{\text{vox}}(-\boldsymbol{k}) \delta_h(-\boldsymbol{k}), \qquad (3.7)$$

where the survey window function is not normalized, so that $\int \mathrm{d}^3 x W_{\text{vol}}(\boldsymbol{x}) = V_{\text{field}}$. Then, we can express the VID as

$$\mathcal{B}_i = N_{\text{vox}} \int_{\Delta T_i} \mathrm{d}T \sum_{N=0}^{\infty} (P_{\text{noise}} * P_N)(T) P_{\text{Poiss}}(N, \bar{N}_h) \left[1 + \frac{(N - \bar{N}_h)}{V_{\text{field}}} \int \frac{\mathrm{d}^3 k}{(2\pi)^3} W_{\text{vol}}(\boldsymbol{k}) W_{\text{vox}}(-\boldsymbol{k}) \delta_h(-\boldsymbol{k}) \right]. \qquad (3.8)$$

IV. VARIANCE AND COVARIANCE

In this section we use the reformulation of the voxel temperature PDF in terms of the local halo overdensity derived in the previous section to compute the variance of the VID and its covariance with the power spectrum.

A. VID

Given a PDF for the voxel temperatures, the *observed* voxel count within each temperature bin ΔT follows a multinomial distribution, since the temperature within a given voxel either lies in a given temperature bin or does not, and different temperature bins are mutually exclusive. The expected value for each bin $\langle \mathcal{B}_i \rangle = \mathcal{B}_i$; hence this is an unbiased estimator, and its variance is $\sigma_{\mathrm{bin},i}^2 = \mathcal{B}_i(1 - \mathcal{B}_i/N_{\mathrm{vox}})$.[2] Nonetheless, due to the dependence of the VID on the density field shown in the previous section, there is an additional contribution σ_{cv}^2 to the variance of $\mathcal{B}_i$ coming from cosmic variance. In addition, different temperature bins are also correlated due to physical processes, which depend on the matter-density field, halo bias and line-luminosity function, correlated sky and noise structures, and processing effects; the modeling of the physical contributions to the off-diagonal covariance of the VID is beyond the scope of this study and is left for future work.

The cosmic variance only affects the astrophysical signal present in $\mathcal{P}(T)$, but it cannot be separated from the instrumental noise contributions in the VID. We therefore compute the covariance for the total VID and not for only the astrophysical contribution. At linear order, we have,

$$\begin{aligned} \sigma_{\mathrm{cv},i}^2 = \sigma_{\mathrm{cv}}^2(\mathcal{B}_i) &= \langle \mathcal{B}_i \mathcal{B}_i \rangle - \langle \mathcal{B}_i \rangle \langle \mathcal{B}_i \rangle \\ &= \frac{N_{\mathrm{vox}}^2}{V_{\mathrm{field}}^2} \Upsilon_i^2 \int \frac{\mathrm{d}^3 \boldsymbol{k}}{(2\pi)^3} W_{\mathrm{vol}}^2(\boldsymbol{k}) W_{\mathrm{vox}}^2(-\boldsymbol{k}) P_h(k) \\ &\equiv \frac{\Upsilon_i^2}{V_{\mathrm{vox}}^2} \sigma_{\mathrm{vol}}^2, \end{aligned} \tag{4.1}$$

where the integral in the second line corresponds to the variance of the halo density field on the survey volume, as indicated in the last line, and we have defined

$$\Upsilon_i = \int_{\Delta T_i} \mathrm{d}T \mathcal{P}_{\mathrm{noise}} * \left(\sum_{N=0}^{\infty} (N - \bar{N}_h) \mathcal{P}_N(T) \mathcal{P}_{\mathrm{Poiss}}(N, \bar{N}_h) \right), \tag{4.2}$$

the sign of which depends on whether the voxel lies on a halo under or overdensity.

We assume that these two contributions to the variance of the VID are independent, and hence the total variance of $\mathcal{B}_i$ is

$$\sigma_{\mathrm{tot},i}^2 = \sigma_{\mathrm{bin},i}^2 + \sigma_{\mathrm{cv},i}^2 = \mathcal{B}_i(1 - \mathcal{B}_i/N_{\mathrm{vox}}) + \Upsilon_i^2 \sigma_{\mathrm{vol}}^2/V_{\mathrm{vox}}^2. \tag{4.3}$$

Both contributions to the covariance of the VID scale generally as V_{field}; note that σ_{cv}^2 only depends on the volume through σ_{vol}^2, which goes roughly as V_{field} (modulo variations due to changes in the shape of the mask window) and that $N_{\mathrm{vox}} \propto V_{\mathrm{field}}$ in the case of σ_{bin}^2. This may be counterintuitive, especially for the contribution coming from cosmic variance. However, note that the VID, as defined in Eq. (2.9), does not involve an average over positions or configurations (as is the case of e.g., the power spectrum). If that were the case, there would be no N_{vox} factor in Eqs. (2.9) and (4.1), and $\sigma_{\mathrm{bin}}^2 \propto N_{\mathrm{vox}}^{-1}$. Similarly, σ_{cv}^2 would scale as V_{field}^{-1}, connecting with the intuition of cosmic variance from other summary statistics. In any case, for any definition of $\mathcal{B}$, both contributions to its variance scale similarly with the volume. Finally, if we observe more than one patch on the sky, we shall divide the variance of the VID by the number N_{field} of fields observed (assuming all of them have the same volume and shape).

As it is evident from Eq. (4.1), σ_{cv}^2 depends on the survey volume, the survey mask and the resolution, as well as σ_N, all of which can vary widely from case to case. However, we can compare as generally as possible the two contributions to the total variance of the VID in Eq. (4.3). Their ratio is given by

$$\frac{\sigma_{\mathrm{cv},i}^2}{\sigma_{\mathrm{bin},i}^2} = \frac{\sigma_{\mathrm{vol}}^2/V_{\mathrm{field}}}{V_{\mathrm{vox}}} \frac{[\int_{\Delta T_i} \mathrm{d}T \mathcal{P}_{\mathrm{noise}} * (\sum_{N=0}^{\infty} (N - \bar{N}_h) \mathcal{P}_N(T) \mathcal{P}_{\mathrm{Poiss}}(N, \bar{N}_h))]^2}{\int_{\Delta T_i} \mathrm{d}T \mathcal{P}_{\mathrm{noise}} * (\sum_{N=0}^{\infty} \mathcal{P}_N(T) \int \mathrm{d}\eta \mathcal{P}_{LN}(\eta) \mathcal{P}_{\mathrm{Poiss}}(N, \eta))}. \tag{4.4}$$

By definition, the two integrals above are smaller than one; in particular, the $(N - \bar{N}_h)$ term makes the integral in the numerator smaller for most N values.

---

[2]The off-diagonal covariance of the VID from the sampling of the PDF is $\sigma_{\mathrm{bin},ij} = -\mathcal{B}_i \mathcal{B}_j/N_{\mathrm{vox}}$. This covariance is always negative because one more voxel within a temperature bin means one less in the rest.

Since that integral is also squared, we expect the second fraction on the right-hand side of Eq. (4.4) to be very small and dominate the first one. Therefore, we expect the cosmic variance contribution to the variance of the VID to be subdominant. We confirm this intuition in Fig. 1, where we show both contributions as functions of the angular resolution (keeping all other parameters and the instrumental noise per voxel fixed) and as
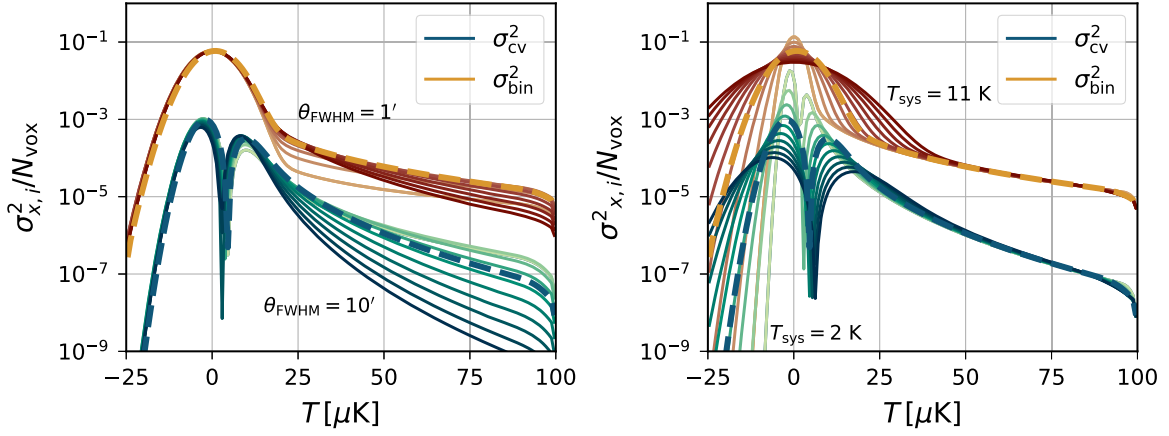
FIG. 1. Comparison of the bin (upper set of curves) and cosmic variance (lower set of curves) contributions to the variance of the VID for our fiducial case (thick dashed lines) and for varying the angular resolution (left) from 1' (dark) to 10' (light) while keeping every other parameter and noise per voxel fixed, and the system temperature (right) from 2 K (dark) to 11 K (light). We divide the variance by the number of voxels in each case to highlight the dependence on the resolution besides the change in the amplitude.

functions of T_{sys}, divided by the number of voxels in both cases.

For most cases, the contribution from cosmic variance is roughly 2 orders of magnitude smaller than σ_{bin}^2. This difference becomes larger at high temperatures as the angular resolution degrades, and it decreases at the temperatures where the VID starts to be dominated by the astrophysical contribution ($\sim 20\ \mu$K in our case) for better angular resolution. As we reduce T_{sys}, the difference between the two contributions decreases at low temperatures. Therefore, this contribution cannot be neglected in cases with good angular resolution and low temperature noise.

B. VID + $P(k)$

A joint analysis of the VID and the LIM power spectrum is key to maximizing the astrophysical and cosmological information recovered from LIM experiments. In order to combine these two observables, it is necessary to model the covariance between them. One can argue that a correlation between the two signals is expected because larger temperature fluctuations result in a more extended PDF for the temperatures, and the other way around. The covariance

between the VID and the power spectrum can therefore be understood as the response of the measured power spectrum to the local density perturbation and luminosity function.

We consider the estimator for the LIM power spectrum monopole P_0 of a wave number k_j, which is given by

$$\hat{P}_0(k_j) = \frac{1}{V_{field}} \int_{V_{k_j}} \frac{d^3 k}{V_{k_j}} \tilde{\delta}_T(\mathbf{k}) \tilde{\delta}_T(-\mathbf{k}), \qquad (4.5)$$

where V_{k_j} is the Fourier-space volume of the jth wave number bin, and $\tilde{\delta}_T$ is the observed brightness temperature perturbation. That is, we have that

$$\tilde{\delta}_T(\mathbf{k}) = \int_{V_{field}} d^3 x\, e^{-i\mathbf{k}\cdot\mathbf{x}} \int d^3 x' W_{vox}(\mathbf{x} - \mathbf{x}') \delta_h(\mathbf{x}')$$

$$= \int \frac{d^3 q}{(2\pi)^3} \delta_T(\mathbf{k} - \mathbf{q}) W_{vox}(\mathbf{k} - \mathbf{q}) W_{vol}(\mathbf{q}). \qquad (4.6)$$

The covariance between the VID and the power spectrum is given by

$$\text{Cov}[\mathcal{B}_i, \hat{P}_0(k_j)] = \frac{N_{vox}}{V_{field}^2} \Upsilon_i \int \frac{d^2 \Omega_{\hat{k}}}{4\pi} \int \frac{d^3 q_1}{(2\pi)^3} \int \frac{d^3 q_2}{(2\pi)^3} \int \frac{d^3 q_3}{(2\pi)^3} W_{vox}(-\mathbf{q}_1) W_{vol}(\mathbf{q}_1) W_{vol}(\mathbf{q}_2)$$

$$\times W_{vox}(\mathbf{k} - \mathbf{q}_2) W_{vol}(\mathbf{q}_3) W_{vox}(-\mathbf{k} - \mathbf{q}_3) \langle \delta_h(-\mathbf{q}_1) \delta_T(\mathbf{k} - \mathbf{q}_2) \delta_T(-\mathbf{k} - \mathbf{q}_3) \rangle. \qquad (4.7)$$

From the definition of the bispectrum, we have that

$$\langle \delta_h(-\mathbf{q}_1) \delta_T(\mathbf{k} - \mathbf{q}_2) \delta_T(-\mathbf{k} - \mathbf{q}_3) \rangle = (2\pi)^3 \delta_D^3(-\mathbf{q}_1 - \mathbf{q}_2 - \mathbf{q}_3) B_{hTT}(-\mathbf{q}_1, \mathbf{k} - \mathbf{q}_2, -\mathbf{k} - \mathbf{q}_3), \qquad (4.8)$$

where the bispectrum above is computed according to Eq. (2.13). Substituting this definition into the expression for the covariance and integrating over $\mathbf{q}_3$ yields

$$\mathrm{Cov}[\mathcal{B}_i, \hat{P}_0(k_j)] = \frac{N_\mathrm{vox}}{V_\mathrm{field}^2} \Upsilon_i \int \frac{d^2\Omega_{\hat{k}}}{4\pi} \int \frac{d^3\boldsymbol{q}_1}{(2\pi)^3} \int \frac{d^3\boldsymbol{q}_2}{(2\pi)^3} W_\mathrm{vol}(\boldsymbol{q}_1) W_\mathrm{vol}(\boldsymbol{q}_2) W_\mathrm{vol}(-\boldsymbol{q}_1 - \boldsymbol{q}_2)$$
$$\times W_\mathrm{vox}(-\boldsymbol{q}_1) W_\mathrm{vox}(\boldsymbol{k} - \boldsymbol{q}_2) W_\mathrm{vox}(-\boldsymbol{k} + \boldsymbol{q}_1 + \boldsymbol{q}_2) B_{hTT}(-\boldsymbol{q}_1, \boldsymbol{k} - \boldsymbol{q}_2, -\boldsymbol{k} + \boldsymbol{q}_1 + \boldsymbol{q}_2). \tag{4.9}$$

Assuming the theoretical model and experimental configuration described in Sec. II, we perform the integral shown above directly, using the VEGAS package [60].

We define the pseudocorrelation matrix between the VID of a temperature bin T_i and the power spectrum monopole of a Fourier mode k_j as

$$c_{ij} = \frac{\mathrm{Cov}[\mathcal{B}_i, \hat{P}_0(k_j)]}{\sigma_{\mathcal{B}_i} \sigma_{P_0(k_j)}}, \tag{4.10}$$

where the standard deviation $\sigma_{P_0(k_j)}$ is computed assuming that the Fourier modes are uncorrelated (see, e.g., Ref. [36]):

$$\sigma_{P_0(k)}^2 = \frac{1}{2} \frac{\int_{-1}^{1} d\mu (\tilde{P}(k,\mu) + P_N)^2}{N_\mathrm{modes}(k)}, \quad \text{with}$$

$$N_\mathrm{modes}(k) = \frac{k^2 \Delta k}{4\pi^2} V_\mathrm{field} N_\mathrm{field}, \tag{4.11}$$

where $N_\mathrm{modes}(k)$ is the number of modes per k bin of width Δk, V_field is the observed volume and N_field is the number of fields observed. The variance in the VID $\sigma_{\mathcal{B}_i}$ is calculated from Eq. (4.3), which includes both the Poisson noise and the effect of cosmic variance. Notice that the pseudocorrelation matrix can be greater than 1 for cases with low instrumental noise due primarily to the shortcomings of the assumed Gaussian power spectrum covariance.

We show in Fig. 2 the expected correlation matrix between the VID and the power spectrum for each wave number and temperature bin. We assume the fiducial

COMAP Y5 configuration described in Sec. II C and consider additional scenarios in which the experiment has lower or higher instrument noise. The effect this has on the power spectrum is to increase or decrease the white noise power due to thermal noise, and the effect it has on the VID is to broaden or narrow the Gaussian distribution of the noise temperature, which is then convolved with the signal.

Let us discuss the main qualitative features of the correlation. First, the correlation matrix is null at the smallest and largest scales probed by the power spectrum; this is due to the limited survey volume and resolution of the experiment. At low temperatures, the VID and the power spectrum are anticorrelated and become correlated as the temperature increases. This can be explained as follows. The VIDs at the lowest temperatures are dominated by the instrumental noise and correspond to the voxels within underdensities for which the astrophysical contribution is the dimmest. These low-temperature bins are anticorrelated with the power spectrum, since a higher power spectrum (i.e., larger temperature fluctuations) widens the astrophysical temperature PDF and the total VID—given by the convolution between noise and astrophysical PDFs—shifts towards higher temperatures. This results in a reduction of the values of $\mathcal{B}_i$ at low temperatures (and a corresponding increase at high temperatures, hence the positive correlation between the power spectrum and the VID). We also notice that the correlation peaks at the temperatures for which the signal-to-noise ratio for the astrophysical contribution to the VID is maximum, and decreases later at higher temperature due to a lower signal-to-noise ratio. Finally, since the
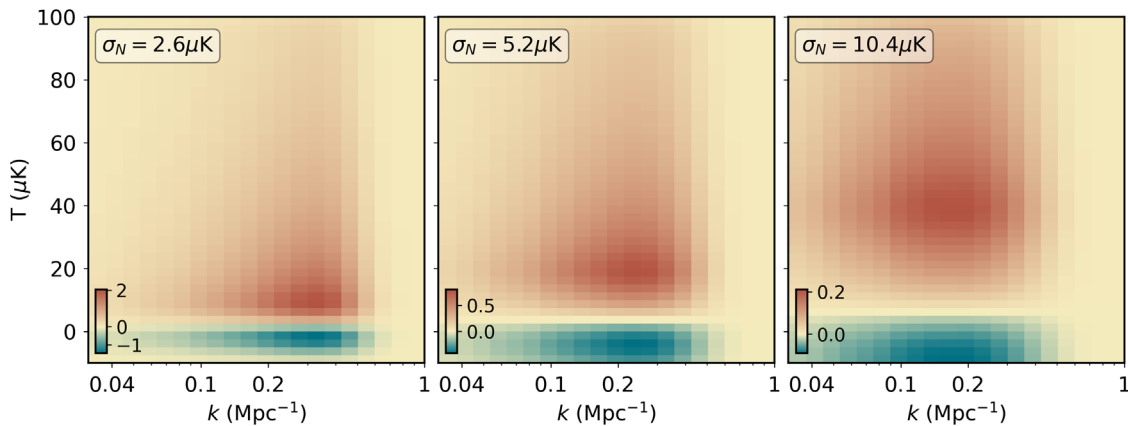
FIG. 2. Value of the pseudocorrelation coefficient between the VID and the power spectrum for different temperature and wave-number bins. The middle panel corresponds to the fiducial scenario described in Sec. II C. The leftmost panel shows the case with half of the noise per voxel and the rightmost panel shows the case with twice the noise per voxel. Notice the different color bars in each panel.

existence of voxels with the highest temperatures depends on the clustering at smaller scales, the correlation decays faster at large scales as the temperature increases.

The general outcome of increasing the noise per voxel is to reduce the correlation coefficient, which is to be expected since the noise is uncorrelated; note that P_N does not appear in Eq. (4.9). We also notice a variety of qualitative changes in the structure of the correlation matrix. As we move from lower to higher instrumental noise, the peak of the correlation matrix shifts from smaller to larger scales. As the noise increases, the wave number k at which the noise power spectrum crosses the signal moves towards larger scales and therefore shifts the peak of the correlation accordingly. As for the variations along the temperature bin, we can see two main effects as the instrumental noise increases: the peak of the correlation shifts towards higher temperatures, and the distribution broadens. The first feature is a consequence of the peak of the signal-to-noise ratio of the VID shifting towards higher temperatures; the second feature is a direct consequence of the broadening of the noise PDF.

Finally, we can directly compare our results with the numerical covariance between the VID and the LIM power spectrum computed in Ref. [46]. We reproduce Fig. 2 in Ref. [46] by adopting the same set of experimental parameters and compute the correlation coefficient as described above. We present this result in Appendix C and find good agreement between the two.

V. CONCLUSIONS

Line-intensity mapping proposes a novel technique that provides access to large cosmological volumes and offers a complementary approach to map large-scale structure, gleaning otherwise inaccessible astrophysical information. Due to the shared dependence on cosmology and astrophysics, the resulting line-intensity maps are very non-Gaussian, and hence leave a significant amount of the information beyond the reach of power spectrum measurements. This is why the VID, which is more sensitive to the line-luminosity function, arises as a very promising summary statistic of LIM observations, especially when also combined with the power spectrum.

We have generalized the VID formalism to account for local variations of the halo density field. This enabled us to derive for the first time an analytic covariance between the LIM power spectrum and the VID—a key step for joint analyses of one- and two-point correlations of line-intensity maps. This approach allows for a faster estimation of the covariance matrix that can be particularly useful when handling problems in which simulations are unavailable or impractical, or that require many evaluations. Furthermore, an analytical approach can offer a deeper understanding of the physical origin of such a covariance, as it clarifies the

connection between the position-dependent PDFs and power spectra. We have also derived the cosmic variance contribution to the variance of the VID, and found that it is a subdominant contribution with respect to the bin variance, with possible exceptions in extreme cases.

We directly compared our results with a simulation-based analysis [46] and found that the results are consistent with each other and that the structure of the correlation matrix is successfully reproduced. While the precision of the results obtained here may be potentially limited by the modeling choices for the VID and power spectrum, the general expression for the covariance, which is given in Eq. (4.9) and is the main result of this work, is general and can be refined with more accurate models. Furthermore, the correlation presented here can be easily extended to a wide range of studies of the statistical properties of intensity maps. Generalizing the covariance for higher-order multipoles of the power spectrum, for higher N-point statistics, or for different tracers of large-scale structure are natural extensions of our results.

The combination of the VID and the LIM power spectrum is expected to significantly improve constraints on theoretical parameters from LIM experiments. In particular, adding the VID to a power spectrum analysis can improve our handle on the line-luminosity function, which helps break the degeneracies between astrophysical uncertainties and cosmological features.

APPENDIX A: SHOT NOISE BISPECTRUM

In this work we consider Poissonian shot noise in all cases. Here we briefly show the derivation of the contribution to the bispectrum B_{hTT}. Consider an infinitesimal volume δV that may contain $N_i = \{0, 1\}$ emitters, where the probability of finding an emitter is $\bar{n}(\boldsymbol{x})(1 + \delta_h(\boldsymbol{x}))\delta V$. Similarly, the expected brightness temperature in that volume is $T_i = N_i X_{\mathrm{LT}} \int \mathrm{d}M L(M) \mathrm{d}n / \mathrm{d}M \delta V / \bar{n}(\boldsymbol{x}) = \langle T(\boldsymbol{x}) \rangle (1 + \delta_T(\boldsymbol{x}))$, with $\delta_T = \delta T / \langle T \rangle$. Under these assumptions, the self-correlators in a given cell are

$$\langle N_i^3 \rangle = \langle N_i^2 \rangle = \langle N_i \rangle = \bar{n}(\boldsymbol{x}_i) \delta V_i,$$
$$\langle T_i^n \rangle = \langle T^n \rangle, \qquad \langle N_i T_i \rangle = \langle T_i \rangle, \qquad \text{(A1)}$$

and the correlators between different cells are

$$\langle n_i n_j \rangle_{i \neq j} = \bar{n}(\boldsymbol{x}_i)\bar{n}(\boldsymbol{x}_j)\delta V_i \delta V_j (1 + \langle \delta_h(\boldsymbol{x}_i)\delta_h(\boldsymbol{x}_j)\rangle),$$

$$\langle n_i n_j n_k \rangle_{i \neq j \neq k} = \bar{n}(\boldsymbol{x}_i)\bar{n}(\boldsymbol{x}_j)\bar{n}(\boldsymbol{x}_k)\delta V_i \delta V_j \delta V_k (1 + \langle \delta_h(\boldsymbol{x}_i)\delta_h(\boldsymbol{x}_j)\delta_h(\boldsymbol{x}_k)\rangle$$
$$+ \langle \delta_h(\boldsymbol{x}_i)\delta_h(\boldsymbol{x}_j)\rangle + \langle \delta_h(\boldsymbol{x}_i)\delta_h(\boldsymbol{x}_k)\rangle + \langle \delta_h(\boldsymbol{x}_j)\delta_h(\boldsymbol{x}_k)\rangle),$$

$$\langle T_i T_j \rangle_{i \neq j} = \langle T(\boldsymbol{x}_i)\rangle\langle T(\boldsymbol{x}_j)\rangle \delta V_i \delta V_j (1 + \langle \delta_T(\boldsymbol{x}_i)\delta_T(\boldsymbol{x}_j)\rangle),$$

$$\langle T_i T_j T_k \rangle_{i \neq j \neq k} = \langle T(\boldsymbol{x}_i)\rangle\langle T(\boldsymbol{x}_j)\rangle\langle T(\boldsymbol{x}_k)\rangle \delta V_i \delta V_j \delta V_k (1 + \langle \delta_T(\boldsymbol{x}_i)\delta_T(\boldsymbol{x}_j)\delta_T(\boldsymbol{x}_k)\rangle$$
$$+ \langle \delta_T(\boldsymbol{x}_i)\delta_T(\boldsymbol{x}_j)\rangle + \langle \delta_T(\boldsymbol{x}_i)\delta_T(\boldsymbol{x}_k)\rangle + \langle \delta_T(\boldsymbol{x}_j)\delta_T(\boldsymbol{x}_k)\rangle). \tag{A2}$$

Now we can compute the multitracer three-point function of interest as

$$\int d^3\boldsymbol{x}_i \int d^3\boldsymbol{x}_j \int d^3\boldsymbol{x}_k \langle N(\boldsymbol{x}_i)T(\boldsymbol{x}_j)T(\boldsymbol{x}_k)\rangle$$
$$= \sum_{i \neq j \neq k} \bar{n}_i \langle T_j \rangle\langle T_k \rangle \delta V_i \delta V_j \delta V_k (1 + \langle \delta_{h,i}\delta_{T,j}\delta_{T,j}\rangle + \langle \delta_{h,i}\delta_{T,j}\rangle + \langle \delta_{h,i}\delta_{T,k}\rangle + \langle \delta_{T,j}\delta_{T,k}\rangle)$$
$$+ \sum_{i=j\neq k} \langle T_i \rangle\langle T_k \rangle \delta V_i \delta V_k (1 + \langle \delta_{T,i}\delta_{T,j}\rangle) + \sum_{i=k\neq j} \langle T_k \rangle\langle T_j \rangle \delta V_k \delta V_j (1 + \langle \delta_{T,k}\delta_{T,j}\rangle)$$
$$+ \sum_{j=k\neq i} \bar{n}_i \langle T_j^2 \rangle \delta V_i \delta V_j (1 + \langle \delta_{h,i}\delta_{T,j}\rangle) + \sum_{i=j=k} \langle T_i^2 \rangle \delta V_i, \tag{A3}$$

where we have converted the integrals in sums and denoted the spatial coordinates with subscripts to save space; the terms in which the sums are constrained to have the same indices correspond to Dirac deltas if we express them as integrals. We are interested in the correlation of the fluctuations:

$$\left\langle \left(\frac{N_i}{\bar{n}} - 1\right)(T_j - \langle T \rangle)(T_k - \langle T \rangle)\right\rangle = \frac{1}{\bar{n}}\langle N_i T_j T_k \rangle - \frac{\langle T \rangle}{\bar{n}}\langle N_i T_j \rangle - \frac{\langle T \rangle}{\bar{n}}\langle N_i T_k \rangle - \langle T_j T_k \rangle + 2\langle T^2 \rangle$$
$$= \langle T \rangle^2 \langle \delta_{h,i}\delta_{T,j}\delta_{T,k}\rangle + \frac{\langle T \rangle^2}{\bar{n}}[\langle \delta_{T,i}\delta_{T,k}\rangle\delta_D^3(\boldsymbol{x}_i - \boldsymbol{x}_j) + \langle \delta_{T,i}\delta_{T,j}\rangle\delta_D^3(\boldsymbol{x}_i - \boldsymbol{x}_k)]$$
$$+ \langle T^2 \rangle\langle \delta_{h,i}\delta_{T,j}\rangle\delta_D^3(\boldsymbol{x}_j - \boldsymbol{x}_k) + \frac{\langle T^2 \rangle}{\bar{n}}\delta_D^3(\boldsymbol{x}_i - \boldsymbol{x}_j)\delta_D^3(\boldsymbol{x}_j - \boldsymbol{x}_k). \tag{A4}$$

Then, by taking the Fourier transform of the expression above to compute the multitracer bispectrum we find

$$B_{hTT}(\boldsymbol{k}_1, \boldsymbol{k}_2, \boldsymbol{k}_3) = B_{hTT}^{\text{clust}}(\boldsymbol{k}_1, \boldsymbol{k}_2, \boldsymbol{k}_3) + \frac{P_{TT}^{\text{clust}}(\boldsymbol{k}_2) + P_{TT}^{\text{clust}}(\boldsymbol{k}_3)}{\bar{n}} + \langle T^2 \rangle\left(\frac{P_{hT}^{\text{clust}}(\boldsymbol{k}_1)}{\langle T \rangle} + \frac{1}{\bar{n}}\right), \tag{A5}$$

as expressed in Eq. (2.13). Similarly, the shot noise for the LIM bispectrum is given by

$$B_{TTT}(\boldsymbol{k}_1, \boldsymbol{k}_2, \boldsymbol{k}_3) = B_{TTT}^{\text{clust}}(\boldsymbol{k}_1, k_2, \boldsymbol{k}_3) + \frac{\langle T^2 \rangle}{\langle T \rangle}[P_{TT}^{\text{clust}}(\boldsymbol{k}_1) + P_{TT}^{\text{clust}}(\boldsymbol{k}_2) + P_{TT}^{\text{clust}}(\boldsymbol{k}_3)] + \langle T^3 \rangle. \tag{A6}$$

APPENDIX B: TREE-LEVEL PERTURBATION THEORY KERNELS AND BIASES

The multitracer bispectrum required to describe the covariance between the VID and power spectrum has contributions from both clustering and shot noise. At tree level, the clustering term can be written as

$$B_{hTT}^{\text{clust}}(\boldsymbol{k}_1, \boldsymbol{k}_2, \boldsymbol{k}_3) = 2\langle T \rangle^2 \{Z_1^h(\boldsymbol{k}_1)Z_1^T(\boldsymbol{k}_2)Z_2^T(\boldsymbol{k}_1, \boldsymbol{k}_2)P_l(k_1)P_l(k_2) + Z_1^h(\boldsymbol{k}_1)Z_1^T(\boldsymbol{k}_3)Z_2^T(\boldsymbol{k}_1, \boldsymbol{k}_3)P_l(k_1)P_l(k_3)$$
$$+ Z_1^T(\boldsymbol{k}_2)Z_1^T(\boldsymbol{k}_3)Z_2^h(\boldsymbol{k}_2, \boldsymbol{k}_3)P_l(k_2)P_l(k_3)\}, \tag{B1}$$

where P_l is the linear matter power spectrum, and Z_1^X and Z_2^X are the redshift-space kernels corresponding to tracers $X = h, T$:

$$Z_1^X(\boldsymbol{k}_i) \equiv (b_1^X + f\mu_i),$$

$$Z_2^X(\boldsymbol{k}_i, \boldsymbol{k}_j) \equiv b_1^X \left[F_2(\boldsymbol{k}_i, \boldsymbol{k}_j) + \frac{f\mu_{ij}k_{ij}}{2} \left(\frac{\mu_i}{k_i} + \frac{\mu_j}{k_j} \right) \right]$$

$$+ f\mu_{ij}^2 G_2(\boldsymbol{k}_i, \boldsymbol{k}_j) + \frac{f^2\mu_{ij}k_{ij}}{2}\mu_i\mu_j \left(\frac{\mu_j}{k_i} + \frac{\mu_i}{k_j} \right)$$

$$+ \frac{b_2^X}{2} + \frac{b_{s^2}^X}{2} S_2(\boldsymbol{k}_i, \boldsymbol{k}_j), \tag{B2}$$

and we use $k_{ij} = |\boldsymbol{k}_i + \boldsymbol{k}_j|$, $\mu_{ij} = (k_i\mu_i + k_j\mu_j)/k$. F_2 and G_2 are the second-order kernels for densities and velocities, and S_2 is the tidal tensor kernel (see, e.g., Refs. [52,61]). Notice that the only difference between tracers in the kernels is through the bias parameters; in the case of the halo density field, the bias parameters are computed with a simple mass average, whereas for the temperature fluctuations, they are also weighted by luminosity:

$$b_\alpha^T(z) = \frac{\int \mathrm{d}M L(M, z) b_\alpha(M, z) \frac{dn}{dM}(M, z)}{\int \mathrm{d}M L(M, z) \frac{dn}{dM}(M, z)}, \tag{B3}$$

where α denotes the bias parameter corresponding to either linear, quadratic, or tidal terms. We compute the halo mass function and the bias parameters $b_\alpha(M, z)$ using the Sheth-Tormen prediction [62,63] and assuming coevolution of halos and dark matter [61,64], so that

$$b_1 = 1 + \epsilon_1 + E_1,$$

$$b_2 = 2\left(1 - \frac{17}{21}\right)(\epsilon_1 + E_1) + \epsilon_2 + E_2,$$

$$b_{s^2} = -\frac{2}{7}(b_1 - 1), \tag{B4}$$

where

$$\epsilon_1 = \frac{\alpha\nu^2 - 1}{\delta_c}, \qquad \epsilon_2 = \frac{\alpha\nu^2}{\delta_c^2}(\alpha\nu^2 - 3),$$

$$E_1 = \frac{2p/\delta_c}{1 + (\alpha\nu^2)^p}, \qquad E_2 = E_1 \left(\frac{1 + 2p}{\delta_c} + 2\epsilon_1 \right). \tag{B5}$$

The shot-noise term in the multitracer bispectrum depends on both P_{hT} and P_{TT}, which we can write using the kernel definitions introduced above as

$$P_{hT}^{\text{clust}}(\boldsymbol{k}) = \langle T \rangle Z_1^h(\boldsymbol{k}) Z_1^T(\boldsymbol{k}) P_l(k), \tag{B6}$$

$$P_{TT}^{\text{clust}}(\boldsymbol{k}) = [\langle T \rangle Z_1^T(\boldsymbol{k})]^2 P_l(k), \tag{B7}$$

where Eq. (B7) is the first term in Eq. (2.12), but rewritten using the kernel Z_1^T.

APPENDIX C: COMPARISON WITH NUMERICAL COVARIANCE

Reference [46] proposed a combined analysis of the VID and the power spectrum using a simulation-based approach. The covariance matrix is obtained by generating a large number of halo catalogs from "peak patch" simulations and assigning CO luminosities based on the model outlined in Ref. [53]. We compare the results derived here with the covariance matrix measured in their work. Adopting the experimental design they define in their Table 1 for the two COMAP phases, a voxel angular size defined by θ_{FWHM}, and the same astrophysical model, we compute the pseudocorrelation matrix using Eqs. (4.3), (4.9), and (4.10), defined as in Ref. [34].

Figure 3 can be directly compared to Fig. 2 in Ref. [46], but we show only the off-diagonal block of the correlation matrix. The first row corresponds to the first stage of the COMAP experiment (COMAP1), the second row corresponds to the second phase (COMAP2), and the third row shows the result in the absence of instrumental noise. The first and second columns in Fig. 3 show the results without and with beam smoothing, respectively.[3] We find good agreement between the two results and that the analytical approach outlined in this work successfully captures the important qualitative features in the correlation.

---

[3]Beam smoothing has no effect on the VID measurements in our modeling of this summary statistic. This is not the case when measuring the VID from a simulated map, since the Gaussian beam extends beyond the size of the voxel.
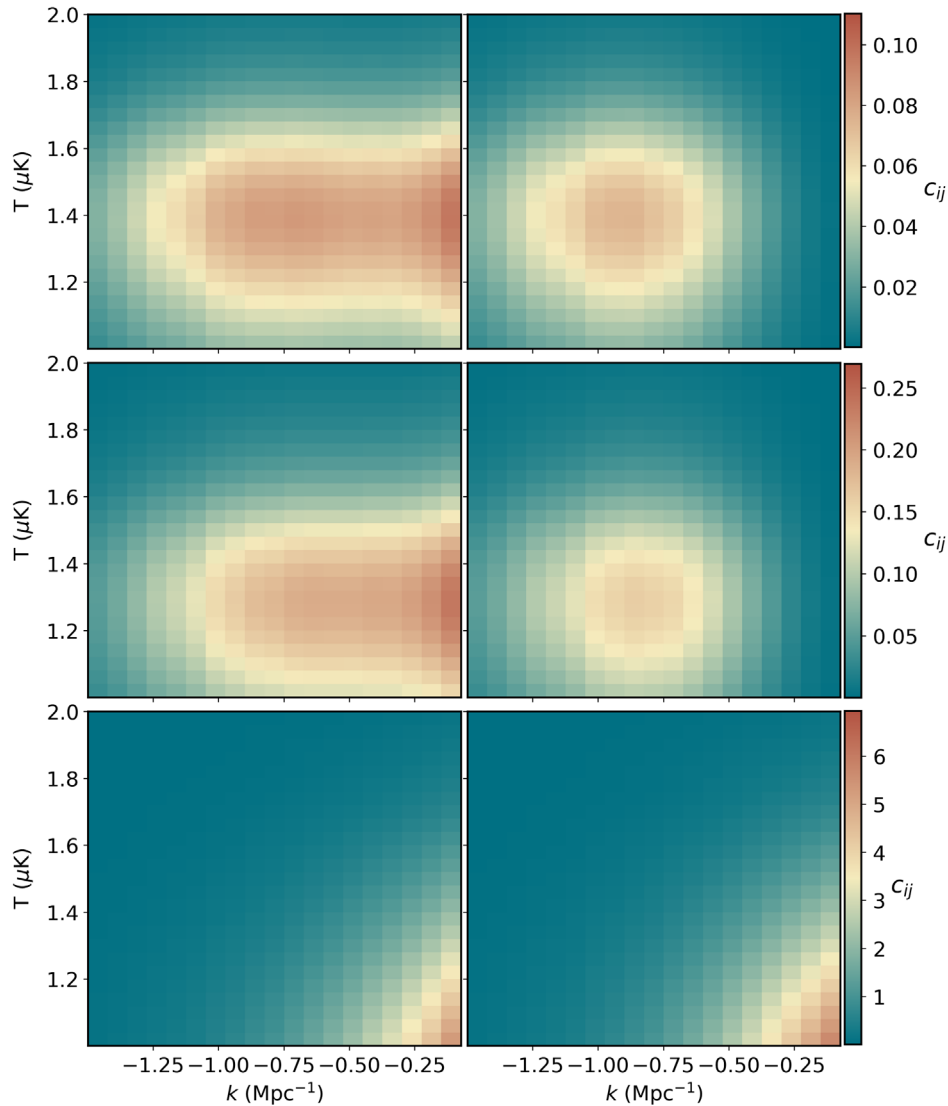
FIG. 3.   Pseudocorrelation matrix between VID and power spectrum that can be directly compared with the simulation-based result from Ref. [46]. The three rows correspond to COMAP1, COMAP2, and signal only, and the left and right columns show the result without and with beam smoothing, respectively.

[1] E. D. Kovetz, M. P. Viero, A. Lidz, L. Newburgh, M. Rahman, E. Switzer *et al.*, Line-intensity mapping: 2017 status report, arXiv:1709.09066.

[2] M. F. Morales and J. S. B. Wyithe, Reionization and cosmology with 21-cm fluctuations, Annu. Rev. Astron. Astrophys. **48,** 127 (2010).

[3] Z. S. Ali *et al.*, PAPER-64 constraints on reionization: The 21 cm power spectrum at $z = 8.4$, Astrophys. J. **809,** 61 (2015).

[4] M. P. van Haarlem, M. W. Wise, A. W. Gunst, G. Heald, J. P. McKean, J. W. T. Hessels *et al.*, LOFAR: The low-frequency array, Astron. Astrophys. **556,** A2 (2013).

[5] S. J. Tingay *et al.*, The murchison widefield array: The square kilometre array precursor at low radio frequencies, Pub. Astron. Soc. Aust. **30,** e007 (2013).

[6] K. W. Masui, E. R. Switzer, N. Banavar, K. Bandura, C. Blake, L. M. Calin *et al.*, Measurement of 21 cm brightness fluctuations at $z \sim 0.8$ in cross-correlation, Astrophys. J. Lett. **763,** L20 (2013).

[7] D. R. DeBoer *et al.*, Hydrogen epoch of reionization array (HERA), Publ. Astron. Soc. Pac. **129,** 045001 (2017).

[8] L. V. E. Koopmans *et al.*, The cosmic dawn and epoch of reionization with the square kilometre array, Proc. Sci., AASKA14 (**2015**) 001 [arXiv:1505.07568].

[9] K. Bandura *et al.*, Canadian hydrogen intensity mapping experiment (CHIME) pathfinder, Proc. SPIE Int. Soc. Opt. Eng. **9145,** 22 (2014).

[10] L. B. Newburgh *et al.*, HIRAX: A probe of dark energy and radio transients, Proc. SPIE Int. Soc. Opt. Eng. **9906,** 99065X (2016).

[11] M. G. Santos *et al.* (MeerKLASS Collaboration), Meer-KLASS: MeerKAT large area synoptic survey, in *MeerKAT Science: On the Pathway to the SKA* (SISSA, Trieste, 2017), arXiv:1709.06099.

[12] A. Lidz, S. R. Furlanetto, S. P. Oh, J. Aguirre, T.-C. Chang, O. Doré, and J. R. Pritchard, Intensity mapping with carbon monoxide emission lines and the redshifted 21 cm line, Astrophys. J. **741,** 70 (2011).

[13] P. C. Breysse, E. D. Kovetz, and M. Kamionkowski, Carbon monoxide intensity mapping at moderate redshifts, Mon. Not. R. Astron. Soc. **443,** 3506 (2014).

[14] T. Y. Li, R. H. Wechsler, K. Devaraj, and S. E. Church, Connecting CO intensity mapping to molecular gas and star formation in the epoch of galaxy assembly, Astrophys. J. **817,** 169 (2016).

[15] A. R. Pullen, T.-C. Chang, O. Doré, and A. Lidz, Cross-correlations as a cosmological carbon monoxide detector, Astrophys. J. **768,** 15 (2013).

[16] H. Padmanabhan, Constraining the CO intensity mapping power spectrum at intermediate redshifts, Mon. Not. R. Astron. Soc. **475,** 1477 (2018).

[17] M. B. Silva, M. G. Santos, A. Cooray, and Y. Gong, Prospects for detecting CII emission during the epoch of reionization, Astrophys. J. **806,** 209 (2015).

[18] A. R. Pullen, P. Serra, T.-C. Chang, O. Dore, and S. Ho, Search for CII emission on cosmological scales at redshift $Z \sim 2.6$, Mon. Not. R. Astron. Soc. **478,** 1911 (2018).

[19] Y. Gong, A. Cooray, M. B. Silva, M. Zemcov, C. Feng, M. G. Santos, O. Dore, and X. Chen, Intensity mapping of Hα, Hβ, [OII], and [OIII] Lines at $z < 5$, Astrophys. J. **835,** 273 (2017).

[20] M. B. Silva, S. Zaroubi, R. Kooistra, and A. Cooray, Tomographic intensity mapping versus galaxy surveys: Observing the universe in H-alpha emission with new generation instruments, arXiv:1711.09902.

[21] A. R. Pullen, O. Dore, and J. Bock, Intensity mapping across cosmic times with the $Ly\alpha$ line, Astrophys. J. **786,** 111 (2014).

[22] M. B. Silva, M. G. Santos, Y. Gong, A. Cooray, and J. Bock, Intensity mapping of Lyα emission during the epoch of reionization, Astrophys. J. **763,** 132 (2013).

[23] K. A. Cleary, J. Borowska, P. C. Breysse, M. Catha, D. T. Chung, S. E. Church *et al.*, COMAP early science: I. Overview, arXiv:2111.05927.

[24] S. K. Choi *et al.*, Sensitivity of the prime-cam instrument on the CCAT-prime telescope, J. Low Temp. Phys. **199,** 1089 (2020).

[25] G. Cataldo, P. Ade, C. Anderson, A. Barlis, E. Barrentine, N. Bellis *et al.*, Overview and status of EXCLAIM, the experiment for cryogenic large-aperture intensity mapping, arXiv:2101.11734.

[26] J. Vieira, J. Aguirre, C. M. Bradford, J. Filippini, C. Groppi, D. Marrone *et al.*, The terahertz intensity mapper (TIM): A next-generation experiment for galaxy evolution studies, arXiv:2009.14340.

[27] O. Doré, J. Bock, M. Ashby, P. Capak, A. Cooray *et al.*, Cosmology with the SPHEREX all-sky spectral survey, arXiv:1412.4872.

[28] G. J. Hill, K. Gebhardt, E. Komatsu, N. Drory, P. J. MacQueen *et al.*, The Hobby-Eberly Telescope Dark Energy Experiment (HETDEX): Description and early pilot survey results, ASP Conf. Ser. **399,** 115 (2008), arXiv:0806.0183.

[29] G. K. Keating *et al.*, First results from COPSS: The CO power spectrum survey, Astrophys. J. **814,** 140 (2015).

[30] G. K. Keating, D. P. Marrone, G. C. Bower, E. Leitch, J. E. Carlstrom, and D. R. DeBoer, COPSS II: The molecular gas content of ten million cubic megaparsecs at redshift $z \sim 3$, Astrophys. J. **830,** 34 (2016).

[31] R. A. C. Croft, J. Miralda-Escudé, Z. Zheng, A. Bolton, K. S. Dawson, J. B. Peterson *et al.*, Large-scale clustering of Lyman α emission intensity from SDSS/BOSS, Mon. Not. R. Astron. Soc. **457,** 3541 (2016).

[32] S. Yang, A. R. Pullen, and E. R. Switzer, Evidence for C II diffuse line emission at redshift $z \sim 2.6$, Mon. Not. R. Astron. Soc. **489,** L53 (2019).

[33] R. P. Keenan, G. K. Keating, and D. P. Marrone, An intensity mapping constraint on the CO-galaxy cross power spectrum at redshift ~3, Astrophys. J. **927,** 161 (2022).

[34] H. T. Ihle *et al.*, COMAP early science: IV. Power spectrum methodology and results, Astrophys. J. **933,** 185 (2022).

[35] H. Padmanabhan, A. Refregier, and A. Amara, Impact of astrophysics on cosmology forecasts for 21 cm surveys, Mon. Not. R. Astron. Soc. **485,** 4060 (2019).

[36] J. L. Bernal, P. C. Breysse, H. Gil-Marín, and E. D. Kovetz, User's guide to extracting cosmological information from line-intensity maps, Phys. Rev. D **100,** 123522 (2019).

[37] P. C. Breysse, E. D. Kovetz, and M. Kamionkowski, The high redshift star-formation history from carbon-monoxide intensity maps, Mon. Not. R. Astron. Soc. **457,** L127 (2016).

[38] P. C. Breysse, E. D. Kovetz, P. S. Behroozi, L. Dai, and M. Kamionkowski, Insights from probability distribution functions of intensity maps, Mon. Not. R. Astron. Soc. **467,** 2996 (2017).

[39] J. L. Bernal, A. Caputo, and M. Kamionkowski, Strategies to detect dark-matter decays with line-intensity mapping, Phys. Rev. D **103,** 063523 (2021).

[40] J. L. Bernal, A. Caputo, F. Villaescusa-Navarro, and M. Kamionkowski, Searching for the Radiative Decay of the Cosmic Neutrino Background with Line-Intensity Mapping, Phys. Rev. Lett. **127,** 131102 (2021).

[41] A. Moradinezhad Dizgah and G. K. Keating, Line intensity mapping with [C II] and CO(1-0) as probes of primordial non-gaussianity, Astrophys. J. **872,** 126 (2019).

[42] J. L. Bernal, P. C. Breysse, and E. D. Kovetz, Cosmic Expansion History from Line-Intensity Mapping, Phys. Rev. Lett. **123,** 251301 (2019).

[43] R. H. Liu and P. C. Breysse, Coupling parsec and gigaparsec scales: Primordial non-Gaussianity with multitracer intensity mapping, Phys. Rev. D **103,** 063520 (2021).

[44] A. Moradinezhad Dizgah, G. K. Keating, K. S. Karkare, A. Crites, and S. R. Choudhury, Neutrino properties with

ground-based millimeter-wavelength line intensity mapping, Astrophys. J. **926,** 137 (2022).

[45] J. B. Bauer, D. J. E. Marsh, R. Hložek, H. Padmanabhan, and A. Laguë, Intensity mapping as a probe of axion dark matter, Mon. Not. R. Astron. Soc. **500,** 3162 (2020).

[46] H. T. Ihle *et al.* (COMAP Collaboration), Joint power spectrum and voxel intensity distribution forecast on the CO luminosity function with COMAP, Astrophys. J. **871,** 75 (2019).

[47] C.-T. Chiang, C. Wagner, F. Schmidt, and E. Komatsu, Position-dependent power spectrum of the large-scale structure: A novel method to measure the squeezed-limit bispectrum, J. Cosmol. Astropart. Phys. 05 (2014) 048.

[48] D. Jamieson and M. Loverde, The position-dependent matter density probability distribution function, Phys. Rev. D **102,** 123546 (2020).

[49] N. Aghanim *et al.* (Planck Collaboration), Planck 2018 results. VI. Cosmological parameters, Astron. Astrophys. **641,** A6 (2020); **652,** C4 (2021)].

[50] P. Coles and B. Jones, A lognormal model for the cosmological mass distribution., Mon. Not. R. Astron. Soc. **248,** 1 (1991).

[51] I. Kayo, A. Taruya, and Y. Suto, Probability distribution function of cosmological density fluctuations from a gaussian initial condition: Comparison of one-point and two-point lognormal model predictions with N-body simulations, Astrophys. J. **561,** 22 (2001).

[52] F. Bernardeau, S. Colombi, E. Gaztanaga, and R. Scoccimarro, Large scale structure of the universe and cosmological perturbation theory, Phys. Rep. **367,** 1 (2002).

[53] T. Y. Li, R. H. Wechsler, K. Devaraj, and S. E. Church, Connecting CO intensity mapping to molecular gas and star formation in the epoch of galaxy assembly, Astrophys. J. **817,** 169 (2016).

[54] M. K. Foss, H. T. Ihle, J. Borowska, K. A. Cleary, H. K. Eriksen, S. E. Harper *et al.*, COMAP early science: III. CO data processing, Astrophys. J. **933,** 184 (2022).

[55] D. T. Chung, P. C. Breysse, K. A. Cleary, H. T. Ihle, H. Padmanabhan, M. B. Silva *et al.*, COMAP early science: V. Constraints and forecasts at $z \sim 3$, Astrophys. J. **933,** 186 (2022).

[56] P. Behroozi, R. H. Wechsler, A. P. Hearin, and C. Conroy, UNIVERSEMACHINE: The correlation between galaxy growth and dark matter halo assembly from $z = 0$–10, Mon. Not. R. Astron. Soc. **488,** 3143 (2019).

[57] D. A. Riechers, R. Pavesi, C. E. Sharon, J. A. Hodge, R. Decarli, F. Walter *et al.*, COLDz: Shape of the CO luminosity function at high redshift and the cold gas history of the universe, Astrophys. J. **872,** 7 (2019).

[58] G. K. Keating, D. P. Marrone, G. C. Bower, E. Leitch, J. E. Carlstrom, and D. R. DeBoer, COPSS II: The molecular gas content of Ten Million cubic megaparsecs at redshift $z \sim 3$, Astrophys. J. **830,** 34 (2016).

[59] D. T. Chung, P. C. Breysse, H. Tveit Ihle, H. Padmanabhan, M. B. Silva, J. R. Bond *et al.*, A model of spectral line broadening in signal forecasts for line-intensity mapping experiments, Astrophys. J. **923,** 188 (2021).

[60] G. P. Lepage, Adaptive multidimensional integration: VEGAS enhanced, J. Comput. Phys. **439,** 110386 (2021).

[61] T. Baldauf, U. Seljak, V. Desjacques, and P. McDonald, Evidence for quadratic tidal tensor bias from the halo bispectrum, Phys. Rev. D **86,** 083540 (2012).

[62] R. K. Sheth and G. Tormen, Large scale bias and the peak background split, Mon. Not. R. Astron. Soc. **308,** 119 (1999).

[63] R. Scoccimarro, R. K. Sheth, L. Hui, and B. Jain, How many galaxies fit in a halo? Constraints on galaxy formation efficiency from spatial clustering, Astrophys. J. **546,** 20 (2001).

[64] K. C. Chan, R. Scoccimarro, and R. K. Sheth, Gravity and large-scale non-local bias, Phys. Rev. D **85,** 083509 (2012).